Journal of Geochemical Exploration 253 (2023) 107293

Contents lists available at ScienceDirect

Journal of Geochemical Exploration

journal homepage: www.elsevier.com/locate/gexplo

Modelling geochemical indices from hyperspectral drill core data from the Eucla Basin basement

Carsten Laukamp [a,*], Emma Beattie [b,1], Monica LeGras [a]

[a] CSIRO Mineral Resources, Australian Resources Research Centre, 26 Dick Perry Avenue, Kensington, WA 6151, Australia
[b] School of Earth and Oceans, James Cook University, Douglas, QLD 4814, Australia

ARTICLE INFO

Keywords:
Partial Least Squares Modelling
PLS
HyLogger
Hyperspectral
Geochemical indices
Eucla Basement

ABSTRACT

Whole rock geochemical analysis of drill core is crucial for rock classification and understanding the evolution of a geological province. This becomes even more important when access to fresh rock samples is hindered by considerable overburden, such as in the case of the basement to the Eucla Basin sediments in Australia. A partial least squares (PLS) regression method was trialled to model geochemical indices, commonly applied for classification of igneous rocks, from hyperspectral visible-near infrared (VNIR; 350 to 1200 nm), shortwave infrared (SWIR; 1200 to 2500 nm) and thermal infrared (TIR; 6000 to 14,500 nm) reflectance spectra of three drill cores intersecting the basement of the Eucla Basin. Modelling of the Mg# (Mg/Mg + Fe) achieved a high correlation between the calculated and predicted values (i.e. $R^2 > 0.9$) at an RMSE of about 10 %. The 2200 to 2400 nm wavelength region of the SWIR was key in modelling the Mg#, with amphibole and chlorite-related absorption features overlapping with the most important input bands in the PLS model. Modelling of the silicon, calcium, iron, magnesium index (SCFM; $SiO_2/(SiO_2 + CaO + FeO + MgO)$) required the TIR wavelength range, where diagnostic spectral signatures of silicates are located. PLS-based modelling of the SCFM achieved even a high correlation (i.e. $R^2 > 0.8$) when the model was developed for one drill core but applied to another drill core that intersects the same lithologies. The third geochemical index trialled was the aluminium saturation index (ASI; $Al_2O_3/(Na_2O + K_2O + CaO)$, producing high correlation between calculated and predicted ASI when using either, the VNIR-SWIR and the TIR wavelength ranges as input. Our study demonstrates how PLS regression can utilise hyperspectral data to determine geochemical indices, without the cost of full geochemical analysis of every sample in a wide array of rock types. The higher spatial resolution of the modelled geochemistry and the extrapolation of the modelling results to intervals that haven't been sampled for geochemistry supports stratigraphic correlation between drill cores. Furthermore, the combined analysis of geochemical and hyperspectrally-derived mineralogy helps mapping the intensity of weathering of basement as well as mineralogical and physicochemical gradients potentially related to hydrothermal systems.

1. Introduction

Geochemical indices derived from whole rock geochemical analysis provide geologists with an improved understanding of the setting and evolution of a geological province. Some of the commonly used geochemical indices for characterisation of igneous rocks comprise the Magnesium Number (Mg#; Mg/(Mg + Fe); (Miyashiro, 1975)); 2) the silicon, calcium, iron, magnesium index (SCFM; $SiO_2/(SiO_2 + CaO + FeO + MgO)$; (Walter and Salisbury, 1989)); and 3) the aluminium saturation index (ASI; $Al_2O_3/(Na_2O + K_2O + CaO)$; (Zen, 1986)).

Lab-based whole rock geochemical analysis, even of major elements, is usually cost-intensive, has a long turnaround time and requires considerable sample preparation. Drill core and handheld instruments can be used for measuring major elements, providing instant access to geochemical data in the field. Even light major elements, such as Na and Mg, which are difficult to measure using X-Ray fluorescence methods, can now also be detected by means of handheld laser-induced breakdown spectroscopy (LIBS; (Day, 2021). However, lab-based whole rock geochemical analysis is still the most common way of accessing reliable geochemistry.

* Corresponding author.
E-mail address: carsten.laukamp@csiro.au (C. Laukamp).
[1] Present address: Geological Survey of Queensland, Department of Resources, 1 William St, Brisbane, QLD 4000.

https://doi.org/10.1016/j.gexplo.2023.107293
Received 18 January 2023; Received in revised form 28 July 2023; Accepted 16 August 2023
Available online 18 August 2023

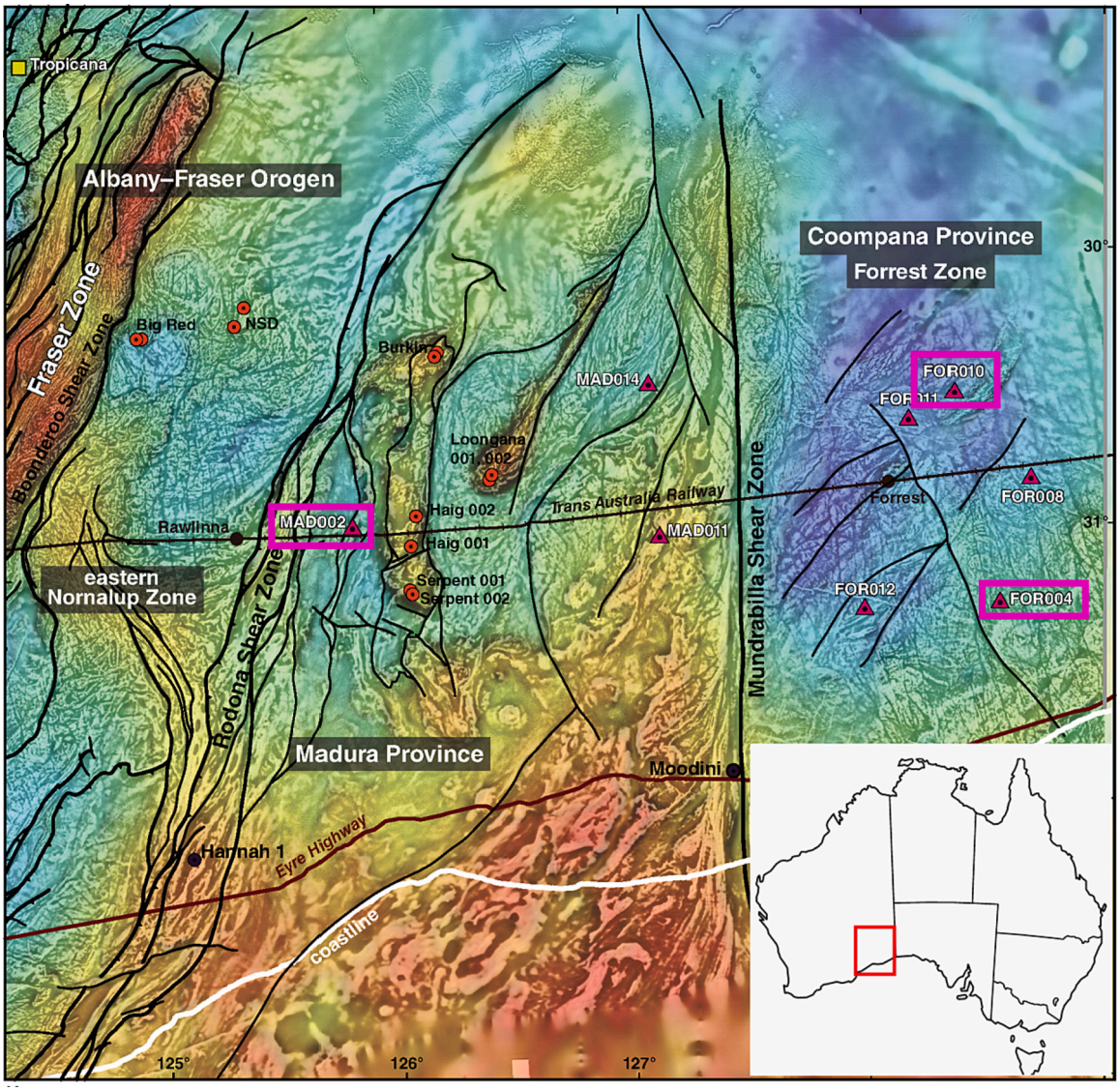

Fig. 1. Gravity image showing Madura and Coompana Provinces of the Eucla Basement separated by the Mundrabilla Shear Zone (Spaggiari and Smithies, 2015) with locations of investigated drill cores highlighted in pink. The study area is highlighted by a red frame in the map of state boundaries of Australia. (For interpretation of the references to colour in this figure legend, the reader is referred to the web version of this article.)

Field and drill core hyperspectral sensing technologies are commonly used for cost-effective and objective characterisation of mineralogy (Laukamp et al., 2021a). Industry and geological surveys are accumulating large amounts of hyperspectral data that have many applications, such as lithological classification, regolith classification, ore body characterisation or vectoring towards hydrothermal ore deposits. The Australian National Virtual Core Library (NVCL) data collection (https://www.auscope.org.au/nvcl), for example, is a publicly available database comprising about 1.6 million reflectance spectra collected from various geological provinces across the Australian continent.

In this study, geochemical indices that can be used to distinguish igneous rock types were calculated from whole rock geochemical results of three drill cores, and modelled from hyperspectral visible-near infrared (VNIR; 350 to 1200 nm), shortwave infrared (SWIR; 1200 to 2500 nm) and thermal infrared (TIR; 6000 to 14,500 nm) reflectance spectra available from the NVCL data collection using a partial least squares modelling approach. The case study area is located in the Western Australian section of the Eucla Basin (Fig. 1). The main objective was to evaluate whether geochemical indices can be modelled from hyperspectral drill core data and whether models developed for one drill core can be applied to other drill cores that intersect the same lithologies. A particular focus of this work was on understanding the causation of any potential correlation between the calculated and predicted geochemical indices. This was based on comparing the final regression factors of the input bands with the vibrational modes of minerals in the respective wavelength ranges that influence the PLS-based modelling of the respective geochemical indices.

1.1. Geology

The Eucla Basin extends laterally over about 2000 km from Western Australia to South Australia, comprising an up to 500 m thick sequence of Tertiary marine, coastal and paleochannel sediments (Benbow et al., 1995; Hou et al., 2008). The basement to the Eucla basin consists of mafic volcanics and a variety of gabbroic to granitic rocks. The understanding of the basement lithologies was limited prior to a drilling program funded by the Geological Survey of Western Australia (GSWA) that initiated extensive geochemical, geochronological and petrographic work, revealing precise information about rock types, age constraints, paragenesis, and providing a regional interpretation of the tectonic setting (Spaggiari and Smithies, 2015). This included visible-near, shortwave and thermal infrared reflectance spectra of six drill cores

Table 1
Mineral assemblages of major basement lithologies according to GSWA and here reported HyLogger, FTIR and XRD analyses.

MAD002			
Supersuite (if allocated by [1])	Rock type/ alteration	GSWA[1]	HyLogger, FTIR and XRD (Laukamp et al., 2021)
	E-MORB	act and/or hbl, plag, ttn* +/− bt, ep, ilm, mgt, qtz,	amph, qtz, wm with layers of increased chl + fsp[#]
	high E-MORB		elevated amph +/− chl; qtz absent
Haig Cave Supersuite	Haig Cave Adakite	bt, plag, qtz +/− act/hbl, sulphides	elevated fsp[#], qtz, wm; low amph, chl
	undifferentiated metabasalt	Amph, ep, plag, qtz	large variety of mineral assemblages
	other alteration mineral assemblages	Plag-Qtz +/− amph, ep veins, sulphides	Epidote and carbonate alteration (mainly in veins) in drill cores that were not labelled. Prehnite alteration in discrete intervals, independent from lithological code, mainly in migmatites
FOR004			
Toolgana Supersuite	granodiorite to monzogranite	bt, hbl, mcl, ocl, plag, qtz, ttn* +/− mgn; alteration minerals: chl, ep, hem, qtz, wm	amph, chl, dm, fsp[#], talc, wm +/− ep, pr
FOR010			
Undawidgi Supersuite	tonalitic metagranite	bt, hbl, plag, qtz; cut by ep-qtz +/− carb, chl veins; mgt altered to hem; interlayered chloritised bt-ep schist	amph, fsp, qtz, wm, iron oxides +/− chl
	Bt-metamonzogranite	bt, fsp +/− bt, mgt, ocl, qtz, sulphides, ttn*, zr*	fsp, qtz, wm, iron oxides +/− chl
Moodini Supersuite	Bottle Corner shoshonite	bt, hbl, Kfsp, plag, qtz, ttn*	Mg-rich amph, fsp, qtz, iron oxides +/− chl; no wm
	Bottle Corner Si-rich shoshonite		fsp, qtz, wm, iron oxides +/− chl, amph (no amph in FOR010!)

Mineral abbreviations: act – actinolite, amph – amphibole, bt – biotite, carb – carbonate, chl – chlorite, dm – dark mica (e.g. biotite), ep – epidote, fl – fluorite, hem – hematite, hbl – hornblende, ilm – ilmenite, Kfsp – K-feldspar, kln – kaolinite; mgt – magnetite, mcl - microcline, ocl – orthoclase, ogl – oligoclase, plag – plagioclase, pr – prehnite, pyr – pyrite, qtz – quartz, ttn – titanite, wm – white mica (e.g. muscovite, phengite), zr - zircon. Minerals are listed alphabetically.
[1]References: (England, 2015; Spaggiari and Smithies, 2015).
ˆ*E*-MORB and high Mg E-MORB were discriminated by GSWA on the base of geochemistry, not mineralogy.
*Mineral groups that are not active in infrared wavelength ranges collected by HyLogger3.
[#]For the hyperspectral drill core data interpretation, feldspar and dark mica mineral species were not discriminated.

collected by means of a Hylogger™3 at the GSWA's Drill Core Library in Perth. Sixteen different Proterozoic igneous units were encountered in the drill cores, with various degrees of alteration. These included enriched mid-ocean ridge basalts (E-MORB), metabasalts, adakites, shoshonites, high-K granites, syenites and diorites, with diverse major, minor and trace element geochemistry indicating a wide array of tectonic settings (Spaggiari and Smithies, 2015-a,b,c). A broad comparison of the mineral assemblages reported by GSWA and the mineral groups and species that were identified by means of HyLogger, Fourier-transform Infrared spectroscopic (FTIR) and X-ray diffraction (XRD) analyses was reported by Laukamp et al. (2021) and is summarised in Table 1. HyLogger-derived mineral assemblages at cm-resolution (i.e. >25,000 data points for drill core MAD002 alone) show a more complex distribution of mineral assemblages – and therefore rock types – than suggested by the lithological codes derived from visual logging.

The three hyperspectral and geochemical drill core data sets investigated for this work intersect the Madura (drill hole MAD004) and Coompana Provinces (drill holes FOR004 and FOR010), which represent the main igneous provinces of the Western Australian section of the Eucla basement.

2. Analytical methods

2.1. Bulk rock geochemistry

Major and minor element geochemistry provided by GSWA was obtained through standard XRF spectrometry of a lithium-fused disc in a platinum mould (Smithies et al., 2015a, b).

2.2. Hyperspectral drill core data

Hyperspectral drill core data as well as high-resolution RGB imagery were collected from the three drill holes MAD002, FOR004, and FOR010 by the GSWA, using a HyLogger3. The HyLogger3 allows rapid acquisition of hyperspectral data from drill core, chips and powders from the visible-near infrared (VNIR, 390–1000 nm), shortwave infrared (SWIR, 1000–2500 nm), and thermal infrared (TIR, 6500–14,500 nm) range of the electromagnetic spectrum (Schodlok et al., 2016). Mineral spectroscopy is based on mineral-specific absorption features, which are largely due to electronic transitions (e.g. ferric iron feature in ferric oxides) or vibrational modes of single bonds or the lattice of a given mineral (e.g. hydroxyl-related combination bands in the 2100 to 2500 nm wavelength range). The wavelength position of absorption features is also influenced by compositional variations within the mineral lattice, for example, anorthite and albite, or the substitution between divalent magnesium and iron in chlorites (for summary see Laukamp et al., 2021). The hyperspectral datasets are publicly available on AuScope's Discovery portal (http://portal.auscope.org/portal/gmap.html) and can be viewed in the The Spectral Geologist (TSG) software (http://www.thespectralgeologist.com/).

3. Partial Least Squares (PLS) regression modelling

Partial Least Squares (PLS) Regression is a statistical technique that models several dependant variables (Y) through a number of predictor variables (X) by relating two data matrices by a linear multivariate model (Wold et al., 2001). The precision of the technique increases with the number of variables and observations and is, therefore, well-suited to matching geochemical variables (Y) with spectral variables (X), while being relatively insensitive to noise.

In geoscience, the PLS modelling approach has been applied mainly to hyperspectral reflectance spectra to predict modal mineral abundance (e.g. Basile et al. 2010; Dalm et al. 2014; Laukamp et al., 2022). However, other case studies have successfully demonstrated the potential for PLS-based modelling of geochemistry, such as total organic carbon (Chang et al., 2005) and even elements in a polymetallic sulphide

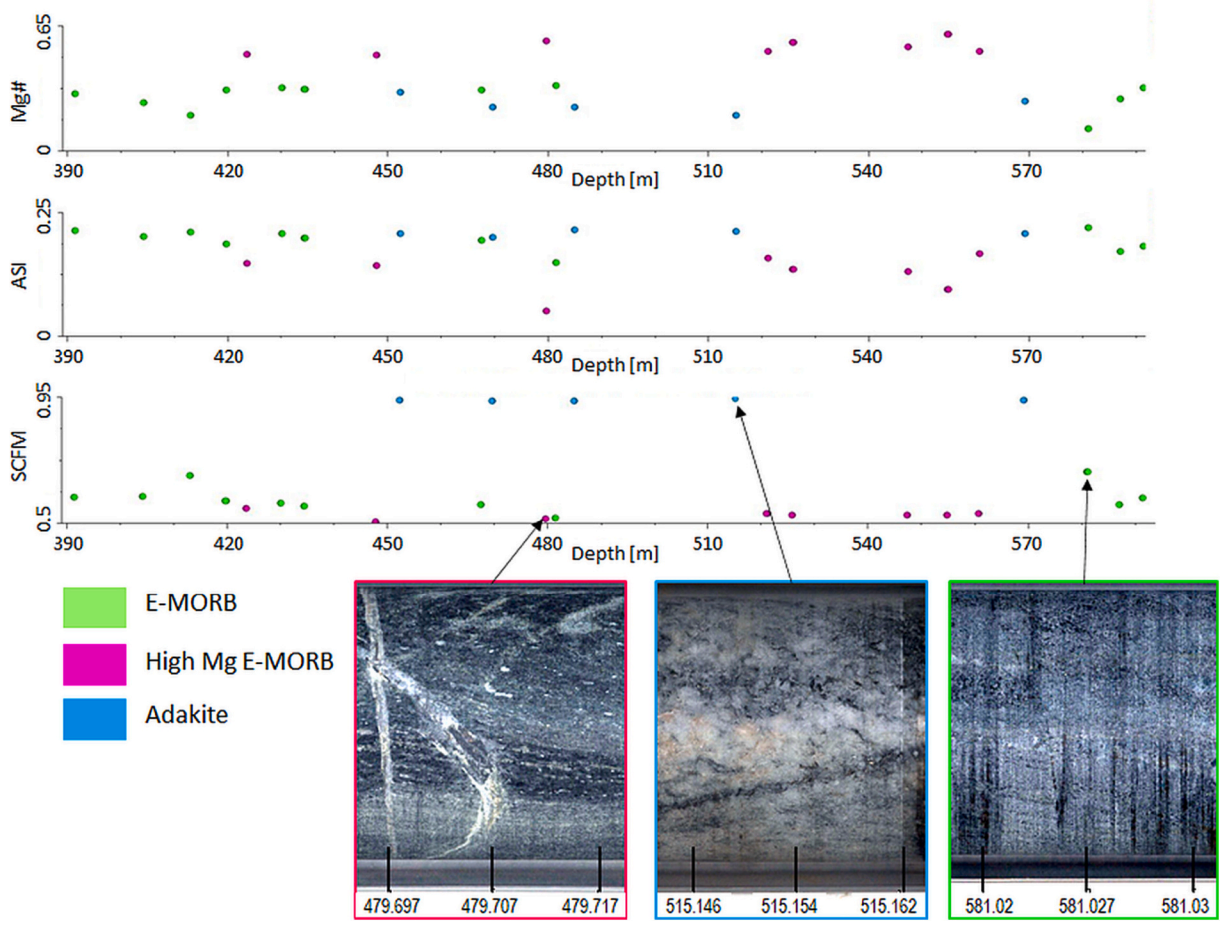

Fig. 2. Downhole plots of Mg# (top), ASI (middle) and SCFM (bottom) calculated from whole rock geochemistry available for MAD002, coloured by the three major lithologies in this drill core: E-MORB (green), High-Mg E-MORB (pink) and adakite (blue). Representative drill core images of each lithology are shown and framed in the colour of the respective class of lithology. (For interpretation of the references to colour in this figure legend, the reader is referred to the web version of this article.)

deposit (Desta et al., 2021), from hyperspectral data. In the context of hyperspectral data, PLS allows qualitative spectra to be converted to modal abundance using an algorithm, using a series of calibration samples (Haaland and Thomas, 1988a, 1988b). The algorithm has properties that combine some of the separate advantages of Classic Least Squares regression (CLS) and Inverse Least Squares regression (ILS), essentially comparing unknown samples (test set) to a reference library (calibration set) and making a prediction that utilises either the full spectral frequency or a subset. In this study, general geochemical indices that distinguish igneous rock types were calculated for the sampled intervals, then modelled to predict the same descriptor in intervals without assays.

It should be noted that PLS relies on the presence of a linear relationship between the variables, and the calibration set used to build the model must be comprehensive enough to fully explain the condition being measured (Ong and Cudahy, 2014). The final regression coefficients (FRC) with the highest absolute values indicate the hyperspectral wavelengths that most influence the model, even if they were not previously known (Ong and Cudahy, 2014).

For this project, the hyperspectral reflectance spectra from drill holes FOR004, FOR010, and MAD002 were trained with geochemistry provided by GSWA and trialled for a PLS-based modelling approach of the following three geochemical indices: 1) Magnesium number ("Mg#"; Mg/(Mg + Fe)), 2) Silica Calcium Iron Magnesium number ("SCFM"; SiO2/(SiO2 + CaO + total FeO + MgO)), and 3) Aluminium saturation index ("ASI"; Al2O3/(Na2O + K2O + CaO)). The TSG™-files containing the PLS-modelling scalars are available via CSIRO's Data Access Portal (Laukamp, 2021); https://data.csiro.au/collections/collection/CIcsiro:50402.

3.1. Summary of PLS workflow

The PLS workflow conducted in TSG™ comprised four main stages: 1. Preparation, 2. Calibration, 3. Prediction, 4. Reporting. The preparation stage included a comparison of the reflectance spectra and their derived mineralogy with the whole rock geochemistry, followed by the selection of calibration samples and the test samples. The calibration stage comprised specification of input data (e.g. wavelength range, background removal), followed by cross-validation. The cross-validation process is based on the leave-one-out method. The predicted residual error sum of squares (PRESS) of the resulting models associated with different numbers of factors are evaluated and the final regression coefficients for each input band (i.e. spectral band) are evaluated. The specification of the input data and the cross-validations steps are iteratively refined. During the prediction stage, the FRC-based scalar is applied to the whole spectral data set and the predicted values are compared with the measured values. It is important to have enough test samples available to make an informed assessment of the accuracy and the precision of the prediction. Like in the case of the calibration samples, the test samples should represent the variability of mineral assemblages and whole value range of the respectively modelled parameter. The reporting stage comprises documenting the parameters that are required to assess the significance of the modelling scalar and predicted values, this includes: 1) wavelength range used for cross

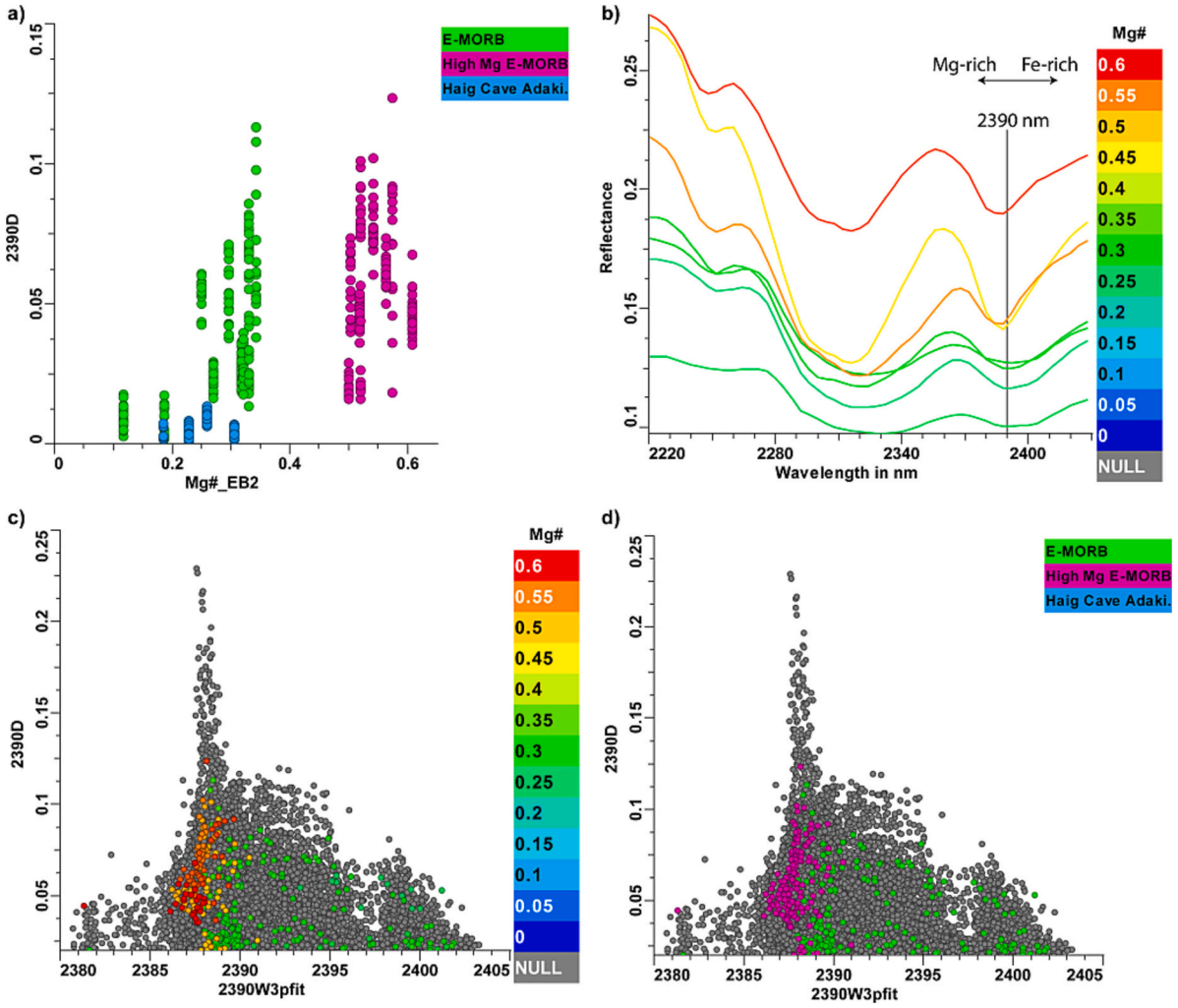

Fig. 3. a) Mg# in drill core MAD002 (x-axis) plotted against the relative intensity of the 2390 nm absorption feature in amphiboles (2390D), coloured by rock type provided by GSWA. b) SWIR reflectance spectra showing major amphibole-related absorption features in the 2200 to 2430 nm wavelength range, coloured by Mg# reported for the respective drill core sample. The central wavelength position of the 2390 nm absorption is highlighted by the vertical line. c) and d): Wavelength position of the 2390 nm absorption (x-axis – 2390W3pfit) versus 2390D (y-axis) coloured by the Mg# and rock type, respectively.

validation; 2) number of calibration and test spectra; 3) value range of modelled parameter; 4) number of factors required to describe the predictive variables (X) chosen to model the dependant variables in the analysis; 5) coefficient of determination, representing the correlation between actual (measured) and predicted for the same observations (samples in the calibration dataset); 6) standard error of prediction (SEP) being the value of the residuals from the linear model; 7) correlation between PLS scalar and measured values, and 9) root mean square error (RMSE) associated with the predicted values.

4. Results – modelling geochemical Indices

Three geochemical indices were modelled from drill cores MAD002, FOR004 and FOR010 using a PLS approach: 1) Magnesium Number (Mg#); 2) SCFM; and 3) ASI. The downhole distribution of the three geochemical indices calculated from whole rock geochemistry of drill core MAD002 is shown in Fig. 2, coloured by the rock type classification. For drill core MAD002, the Mg# is highest in samples classified as High Mg *E*-MORB and the ASI is highest for samples logged as E-MORB and adakite (Fig. 2). ASI values for the High Mg *E*-MORB samples are highly variable. Adakites show the by far highest SCFM values, whereas *E*-MORB and High Mg E-MORB show both very low SCFM values.

4.1. Magnesium number

The magnesium number (Mg#) is a ratio between magnesium and total iron (Eq. (1)), a well-described substitution in most mafic minerals due to the comparable ionic radii, charge and abundance. The Mg# can be used to distinguish between tholeiitic and calc-alkaline series magmas, differentiated by the valency of iron, controlled by oxygen fugacity, and is in turn, diagnostic of tectonic setting (Miyashiro, 1975). In the context of this study, it is trialled as a potential metric to identify and distinguish mafic rock types.

For drill core MAD002, the Mg# is highest in the High Mg E-MORB samples, whereas Mg# values for E-MORB and adakite samples are lower (Fig. 2). Based on petrographic and hyperspectral data (C. Laukamp et al., 2021; Spaggiari and Smithies, 2015), mafic rocks in drill core MAD002 are rich in amphiboles and chlorite/dark micas. The abundance of amphiboles, chlorites and dark micas in mafic rocks increases with increasing Mg#. The correlation between amphibole abundance, derived from hyperspectral data by measuring the relative intensity of the major SWIR-active absorption feature in amphiboles at around 2390 nm ($\nu + \delta$M-O-H), and the Mg# is shown in Fig. 3a. The wavelength position of the amphibole-related absorption feature at around 2390 nm is dependent on the composition of octahedrally coordinated cations in amphiboles, with Mg-rich amphiboles absorbing at

Table 2
MAD002 input parameters for Mg# and important absorption features. TSGTM-files containing the PLS-models can be found in (Laukamp, 2021). The wavelength range for both models was the whole VNIR-SWIR.

Value range (Mg #)	Number of calibration / test spectra	Factors	Coefficient of determination	SEP	Correlation between PLS scalar and measured values	RMSE
0.117–0.608	487/n.a.	14	0.867	0.0511	0.943	0.0465
0.185–0.573	254/233	11	0.929	0.041	0.918	0.0511

shorter wavelengths when compared to Fe-rich amphiboles (Fig. 3b; e.g. (Laukamp et al., 2012)). A bimodal distribution of amphibole composition can be observed in samples classified as E-MORB (long wavelength 2390 nm absorption = Fe-rich) and High Mg E-MORB (short wavelength 2390 nm absorption = Mg-rich) (Fig. 3c, d). Based on the SWIR hyperspectral data, the Haig Cave Adakite contains chlorite and/or biotite, but no amphiboles.

Based on the above comparison of the Mg# with the hyperspectrally-derived mineralogy and the observed correlation of Mg# with relative abundance of SWIR-active minerals, the SWIR wavelength range was used for the PLS-based modelling of the Mg#. The settings for the PLS-based modelling of the Mg# and prediction results are listed in Table 2. The Mg# in MAD002 was modelled using (1) the whole available geochemistry data set for calibration are presented ($n = 487$), and (2) using half the test samples for calibration ($n = 254$). Using the full set of samples with available geochemistry (i.e. 487 samples), a 14 factor model achieved a sufficiently low PRESS (Fig. 4a), whereas only 11 factors were required when using half the geochemistry samples for calibration. Also, the coefficient of determination was higher and the standard error of prediction (SEP) was lower in the 2nd modelling exercise (Table 2). However, the correlation between the resulting PLS-modelling scalars and the measured values was significantly higher (0.943) and the RMSE lower (0.0465) when using the full data set for calibration (*Fig. 4*d, e). The final regression coefficients across the full VNIR-SWIR wavelength range (i.e. across all input bands) highlights the significance of the 2200 to 2450 nm wavelength region (i.e. bands 456 to 516) for modelling the Mg# (Fig. 4c). This wavelength range coincides with strong absorption features of amphibole, chlorite and dark mica – the same minerals that were found to be correlated with changes in the Mg# found in the different rock types of MAD002. The High Mg E-MORB samples can clearly be separated from E-MORB and Haig Cave Adakite samples by using the measured or the modelled Mg# values (Fig. 4d, e). Fig. 4f shows the modelled Mg# emphasizes the bimodal distribution of amphibole compositions, with Mg-rich amphibole samples belonging to the High Mg E-MORB and the Fe-rich amphibole samples to E-MORB.

The prediction of Mg# downhole for the setting using all available calibration samples is shown in Fig. 5c, identifying intervals that haven't been analysed geochemically, but are characterised by a high Mg# number. Application of the most accurate scalar to an unrelated set of rocks (FOR004 and FOR010) was relatively successful, with correlations between actual and predicted values of 0.71 and 0.79, respectively. One set of outliers from the correlation appeared to be due to the iron contribution from sulphides in the samples.

4.2. SCFM

(Walter and Salisbury, 1989) found that the wavelength shifts of thermal infrared-active vibrational modes of silicates was related to depolymerisation of the SiO4 tetrahedra and the subsequent lengthening of the Si—O bonds, influenced by cations such as Ca, Fe and Mg. The SCFM (Si, Ca, Fe, Mg) number provides a ratio between silica and these major cations, and in turn, is useful for discriminating igneous rocks according to their major element contents. It should be noted however, that the SCFM number was developed for unaltered igneous rocks, and siliceous overprints can impact results significantly (Salisbury and D'Aria, 1989). The SCFM index clearly separates adakites from both E-MORB types (Fig. 2), the latter ones having very similar, low SCFM values.

The SCFM was calculated from whole rock geochemical data for drill cores FOR004, FOR010 and MAD002 and modelled with various parameters using the TIR wavelength range (Table 3). The TIR wavelength range was used for modelling the SCFM instead of the SWIR wavelength range, as most of the major mineral groups that contribute to the SCFM show distinct absorption features in the TIR, whilst they are inactive in the SWIR (e.g. quartz, feldspar; (Carsten Laukamp et al., 2021b)). Furthermore, the Christiansen frequency, a TIR reflectance minimum at the short-wavelength side of the primary reststrahlen peaks (Conel, 1969), shifts to longer wavelengths from felsic to mafic minerals, suggesting a good correlation between TIR hyperspectral signatures and the SCFM. Representative TIR reflectance spectra of silicate-bearing samples in drill core FOR010 and MAD002 and the apparent shift of the Christiansen Minimum are shown in Fig. 6a and d. The correlation between the SCFM values and the wavelength position of the Christiansen Minimum in FOR010 are shown in Fig. 6b.

When using all reflectance spectra with available geochemical values in drill core FOR010 for calibration (i.e. 1194), an 18 factor model achieves a high coefficient of determination at 0.918 at a comparably low SEP of 0.0282 (Table 3; model FOR010 A3). The correlation between the SCFM values calculated from whole rock geochemistry and the predicted SCFM values for said PLS model (Fig. 7a) is very high (0.965) and the RMSE very low (0.0258). Outliers in the comparison of the originally calculated SCFM with the predicted values typically represent veins or other samples intervals anomalous to the major rock types present in drill core FOR010 (e.g. 494.88 m depth; see full tsg file for core images). The Bottle Corner Shoshonite (green in Fig. 7b) has the lowest SCFM, compared to the Undawidgi High-K Granite (pink) and Undawidgi Sodic Granite (brown). The Bottle Corner Si-rich Shoshonite (blue) has the highest SCFM values. When training the hyperspectral drill core data with only half of the calibration samples (model FOR010 A4), the correlation between the measured values and the PLS scalar (Table 3; Fig. 7c,d) is still very high (0.95) and the RMSE only increases slightly (0.0358). When reducing the wavelength range, similarly high correlation between measured and predicted SCFM values can be achieved (Table 3; Fig. 7e,f).

Plotting the final regression coefficient (FRC) per each input band highlights that certain wavelength intervals have a higher impact on the modelling than others (Fig. 6c). For example, the 10,425 to 10,975 nm wavelength region (input bands 178 to 200) shows distinct changes between very positive and very negative FRCs, implying that changes in the spectral signature in this wavelength range are related to changes in relative amounts of minerals that are active in this wavelength region. The 10,000 to 11,000 nm wavelength region is sensitive to a large of range silicates, including feldspars, sheet silicates and amphiboles (Fig. 6a). Therefore, any changes with regards to the relative amounts of these minerals directly reflect changes of the SCFM.

When using all reflectance spectra with available geochemical values in drill core MAD002 for calibration (i.e. 487), an 16 factor model achieves a high coefficient of determination at 0.945 at a comparably low SEP of 0.0336 (Table 3; model MAD002 Cal487). The correlation between the SCFM values calculated from whole rock geochemistry and the predicted SCFM values for said PLS model (Fig. 8a) is very high (0.981) and the RMSE very low (0.0271). As with drill core FOR010, outliers in the comparison of the originally calculated SCFM (x-axis in Fig. 8d) with the cross-validated values (y-axis in Fig. 8d) typically represent veins or other sample intervals anomalous to the major rock

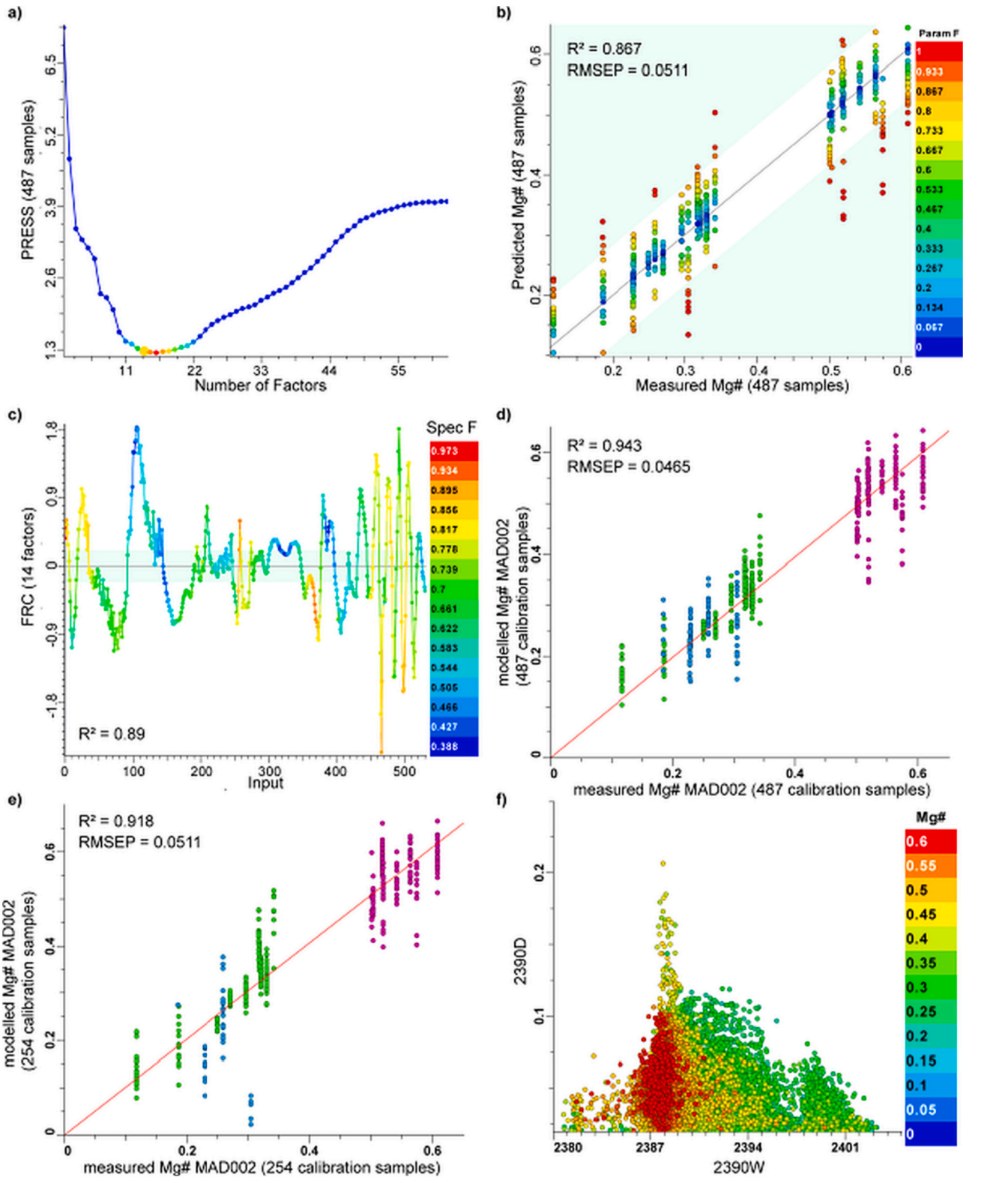

Fig. 4. a) Predicted Residual Error Sum of Squares (PRESS) for PLS-based modelling of Mg# using all available calibration samples in MAD002; b) Comparison of actual (x-axis) and predicted (y-axis) Mg# values for assayed intervals. c) VNIR and SWIR wavelengths (shown as input bands) of most importance based on Final Regression Coefficient (FRC); Comparison of measured Mg# and predicted Mg# using a PLS-based scalar, coloured by rock type, using all available samples for calibration in d) and using half of available assays in e); Wavelength position of the 2390 nm absorption (x-axis – 2390 W) versus relative intensity of the 2390 nm absorption feature in amphiboles (2390D - y-axis) coloured by the PLS-modelling derived Mg# (487 calibration samples).

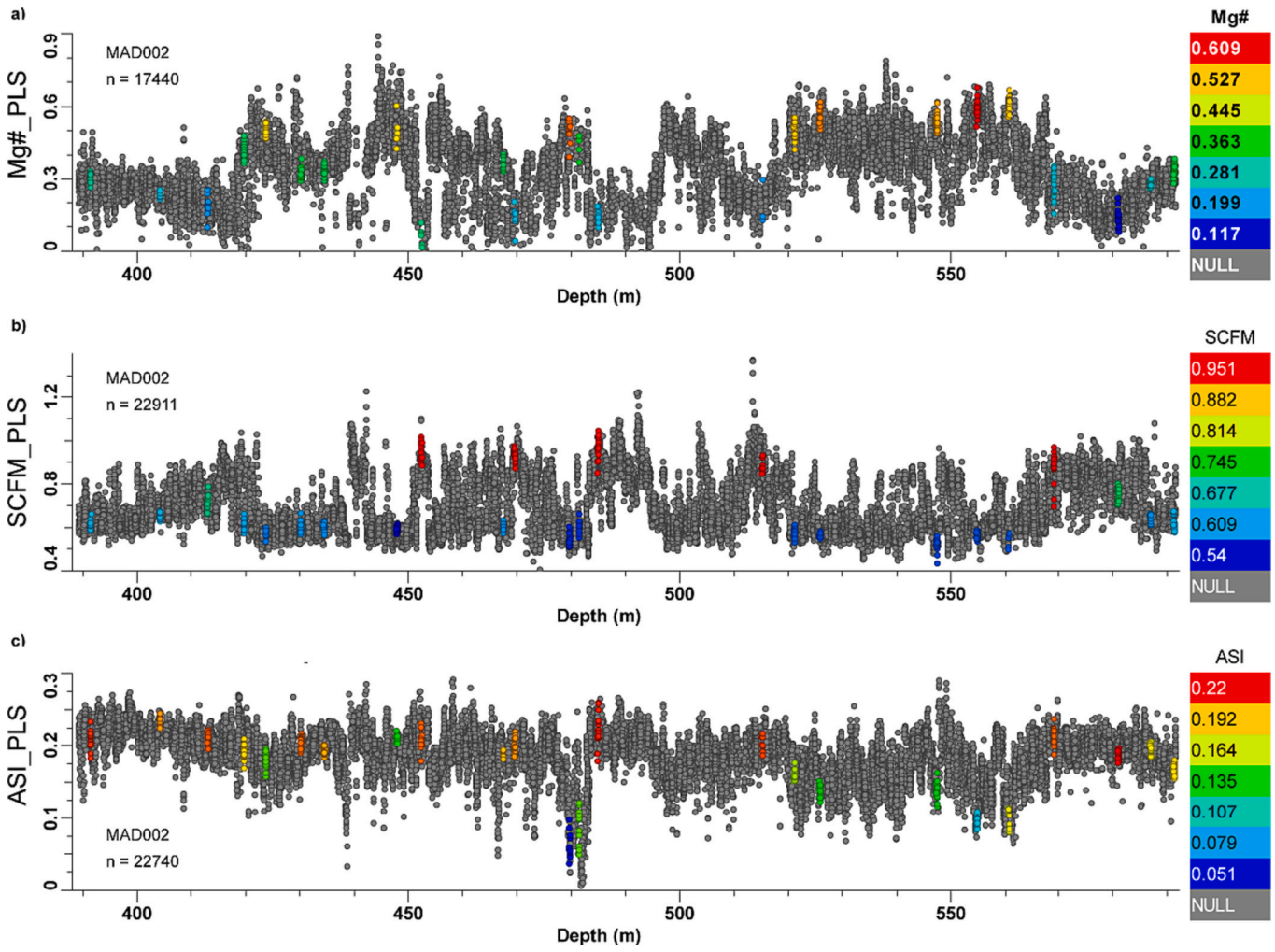

Fig. 5. Comparison of actual (colour scale) and predicted (y-axis) geochemical indices downhole (x-axis) for drill core MAD002: a) Mg#, b) SCFM, c) ASI.

Table 3
FOR010 and MAD002 input parameters for PLS-based modelling of SCFM. TSG™-files containing the PLS-models can be found in (Laukamp, 2021).

Preparation stage			Calibration stage				Prediction stage	
Drill core [PLS model]	Wavelength range [nm] for cross-validation	Value range SCFM	Number of calibration & test spectra	Factors	Coefficient of determi-nation	SEP	Correlation between PLS scalar and measured values	RMSE
FOR010 [A3]	6000–14,500	0.56–0.97	1194 / n.a.	18	0.918	0.0282	0.965	0.0258
FOR010 [A4]	6000–14,500	0.56–0.97	537 / 651	16	0.911	0.0261	0.950	0.0358
FOR010 [A5]	6000–13,200	0.56–0.97	531 / 618	18	0.915	0.0255	0.948	0.0345
FOR004 [A3]	6000–14,500	0.667–0.966	621/50116	15	0.864	0.0369	0.949	0.0317
MAD002 [Cal487]	6000–14,500	0.54–0.95	487 / n.a.	16	0.945	0.0336	0.981	0.0271
MAD002 [Cal240]	6000–14,500	0.54–0.95	240/ 223	14	0.935	0.0377	0.961	0.043

types present in drill core FOR010 (see full tsg file for core images). Also when using about half the available training data, the scalars generated from the PLS modelling of the SCFM show a good correlation with the originally calculated SCFM for the calibration and test data sets (Table 3; Fig. 8c,d). However, the number of calibration samples with SCFM values above 0.65 is insufficient for reliable modelling. Therefore, strictly speaking, the model should be generated and applied in MAD002 only for SCFM values between 0.5 and 0.65.

The wavelength region between 10,425 to 10,975 nm, which had a significant impact on the modelling of the SCFM for drill core FOR010, is less important in drill core MAD002, where the wavelength region between 7875 nm and 8250 nm (input bands 75 to 91) is the most important one for modelling SCFM (Fig. 6e). The latter wavelength region is corresponding to the Christiansen Minimum of silicate minerals, which is located at a different wavelength range dependant on the types of major silicate minerals present in igneous rocks (Walter and Salisbury, 1989).

In downhole plots of the modelled SCFM in drill core MAD002, intervals with elevated SCFM correspond to adakites, whereas intervals with low SCFM correspond to *E*-MORB. Adakites contain more felsic silicates when compared to E-MORB, with felsic minerals dominating the TIR reflectance spectra of adakite and mafic minerals dominating the TIR reflectance spectra of E-MORB. However, there are lot of variations and gradients within the major lithologies and transitions from adakite

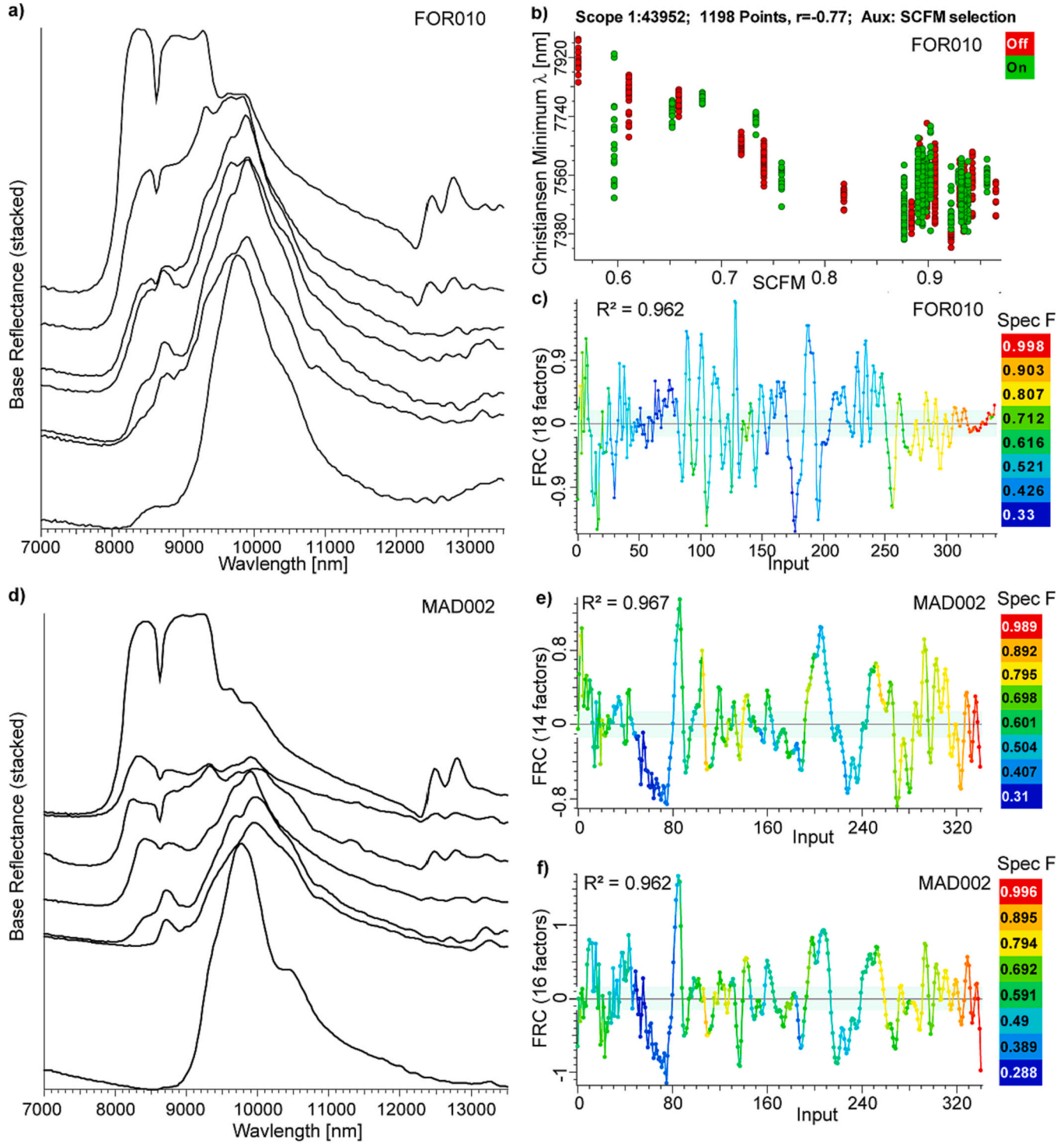

Fig. 6. a) Representative TIR reflectance spectra collected from drill core FOR010 samples that contain large amounts of silicate minerals, showing the shift of the Christiansen Minimum to longer wavelengths from top to bottom (from around 7800 nm to 8200 nm); b) SCFM calculated from whole rock geochemical data (x-axis) versus wavelength position of Christiansen Minimum (y-axis), coloured by samples selected for training ("on", green) and testing ("off", red); c) Final Regression Coefficient (FRC) associated with TIR input bands. d) Representative TIR reflectance spectra collected from drill core MAD002 samples that contain large amounts of silicate minerals, showing the shift of the Christiansen Minimum to longer wavelengths from top to bottom (from around 7800 nm to 9000 nm); e), f) Final Regression Coefficient (FRC) associated with TIR input bands for PLS model MAD002_ Cal487 and MAD002_CAL240, respectively. (For interpretation of the references to colour in this figure legend, the reader is referred to the web version of this article.)

to E-MORB can be gradational too (Fig. 5a).

PLS-modelling of the SCFM for drill core FOR004 was conducted in the same way as described above for drill cores FOR010 and MAD002. A comparison between the SCFM values calculated from whole rock geochemistry and the scalar generated from the PLS-modelling (Fig. 9a) produces a significant correlation ($r = 0.949$). The Toolgana Monzodiorite is characterised by the lowest SCFM values (both, calculated from whole rock geochemistry and modelled), whereas the Intrusive

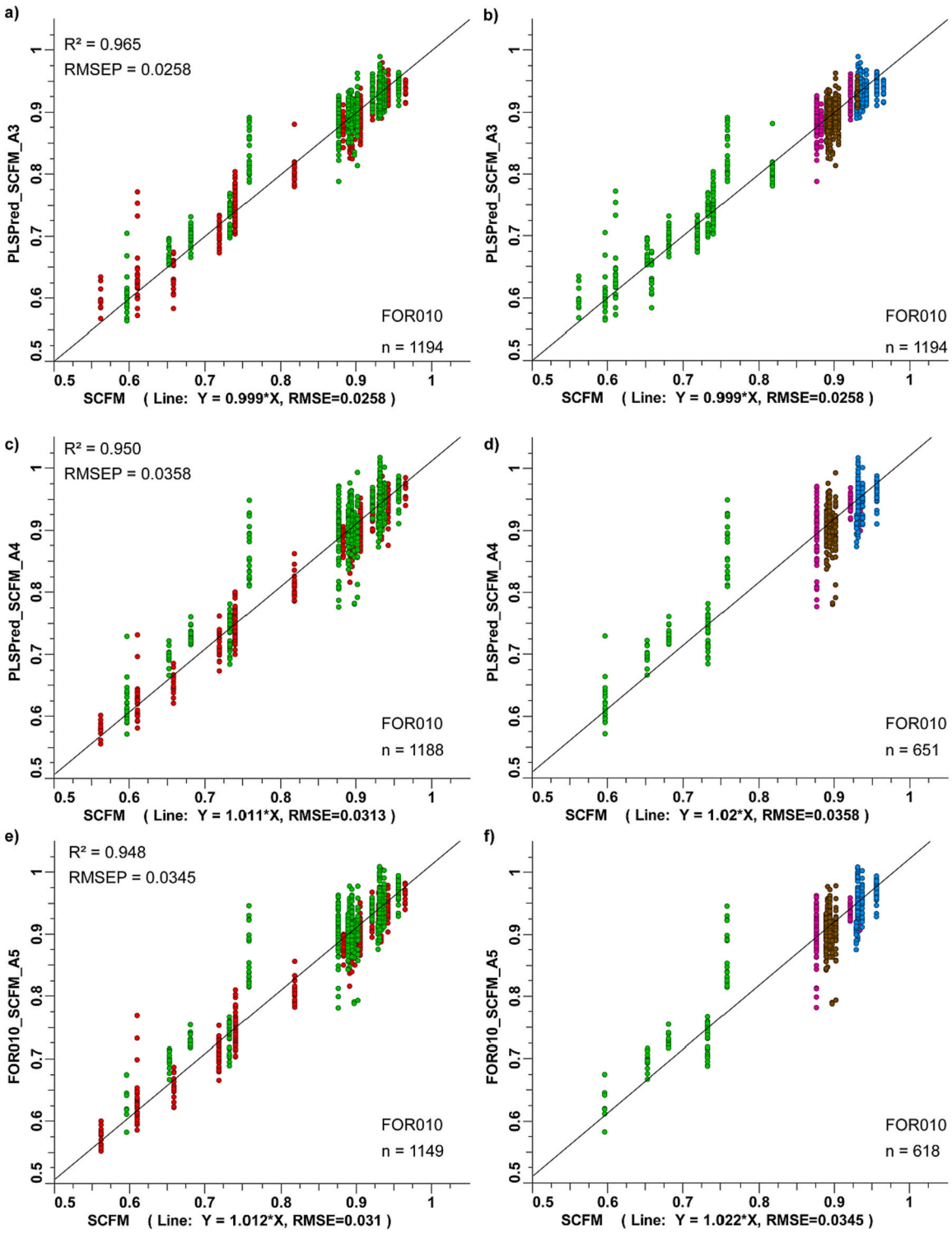

Fig. 7. PLS-based modelling of SCFM for drill core FOR010 using three different amounts calibration/test data and subsets of the TIR wavelength range as described in Table 3: PLS model FOR010_A3 in a) and b), PLS model FOR010_A4 in d) and e), PLS model FOR010_A5 in e) and f). All plots show SCFM calculated from whole rock geochemical data (x-axis) versus predicted SCFM based on respective PLS model (y-axis); a), c) and e) are coloured by calibration (red) / test (green) sample classification; b), d) and f) coloured by rock types: green: Bottle Corner Shoshonite, pink: Undawidgi High-K Granite, brown: Undawidgi Sodic Granite, blue: Bottle Corner Si-rich Shoshonite. (For interpretation of the references to colour in this figure legend, the reader is referred to the web version of this article.)

Anatectic Granite has the highest SCFM values. However, there's considerable overlap between one sample interval of the Toolgana Granodiorite (tray 107: 569.8 to 570.0 m depth) and the Intrusive Anatectic Granite. A downhole plot of the modelled SCFM values of drill core FOR004 (Fig. 9c) shows drill core intervals that have very low and very high values that were not sampled by GSWA for whole rock geochemistry, but that could probably be assigned to the Toolgana Monzodiorite and the Intrusive Anatectic Granite, respectively.

Drill core FOR010 intersects the same lithologies as drill core FOR004. The PLS-based SCFM scalars developed for drill core FOR010 were applied directly to drill core FOR004, producing a significant correlation ($r = 0.838$) between the SCFM values calculated from whole

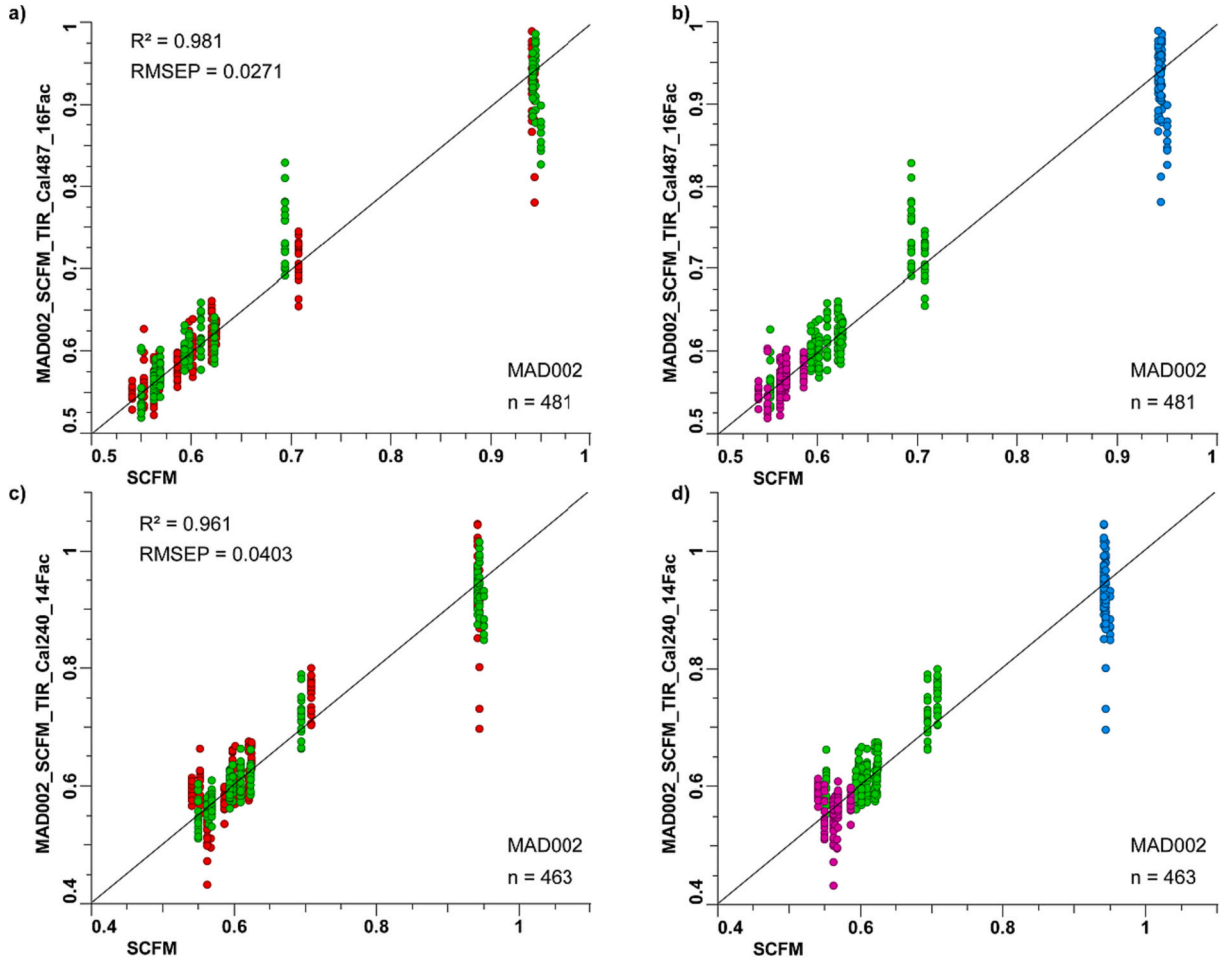

Fig. 8. PLS-based modelling of SCFM for drill core MAD002 using two different amounts calibration/test data as described in Table 3: PLS model MAD002_ Cal487 in a) and b), PLS model FOR010_A5 in f) and g). Plots c) to d) show SCFM calculated from whole rock geochemical data (x-axis) versus predicted SCFM based on respective PLS model (y-axis); d) and f) are coloured by calibration (red) / test (green) sample classification; e) and g) coloured by rock types: green: E-MORB, pink: High-Mg E-MORB, blue: Haig Cave Adakite. (For interpretation of the references to colour in this figure legend, the reader is referred to the web version of this article.)

rock geochemistry analysed in drill core FOR004 on one side (x-axis in Fig. 9b) and the SCFM scalar developed for FOR010 on the other side (y-axis in Fig. 9b). The full range of SCFM values modelled for the Toolgana Monzodiorite overlaps with the calculated value ranges of all other three rock types in this drill core. However, the overall trend of the modelled SCFM in the downhole plot (Fig. 9d) is similar for both PLS-scalars applied to the same drill core FOR004. Also, most of the very low SCFM values are modelled by both PLS-scalars in the same way.

4.3. Aluminium Saturation Index

The Aluminium Saturation Index (Zen, 1986) is used widely to discriminate peraluminous from metaluminous and peralkaline granitic rocks. (Chappell and White, 1992) demonstrated that the extent of aluminium saturation could be used to differentiate between granites in the Lachlan Fold Belt and that the ASI was diagnostic of whether the granite resulted from melting an igneous or sedimentary rock. The aluminium content in granites is chiefly controlled by feldspars and white micas, which have greater abundance in sedimentary rocks than in mafic protoliths. Most felsic units in the here investigated drill cores have been described as A-type under this scheme (Spaggiari and Smithies, 2015), meaning they are potassic, and ferroan alkali-calcic to ferroan alkalic.

The ASI was modelled for drill cores FOR004 and MAD002 (Table 4) using the VNIR-SWIR wavelength range, where hydroxyl-related absorptions related to white and dark micas occur. For comparison, the ASI for drill core MAD002 was also modelled using the TIR wavelength range, which is sensitive to both mineral groups, micas and feldspars.

The best results of PLS modelling ASI from VNIR-SWIR reflectance spectra for drill cores MAD002 (Fig. 10a to c) and FOR004 (Fig. 10d to f) were achieved using 16 and 11 factors, respectively. For both drill cores, the wavelength range between 2100 and 2450 nm (input bands between 430 and 500; Fig. 10c and f) as well as the hydroxyl-related overtone region at around 1400 nm (input bands 255 to 265) have a significant impact on the modelling. This confirms the importance of variations of the sheet silicate content for modelling the ASI. However, it should be noted that the FRC shows significantly stronger variations when modelling the ASI for drill core FOR004 (Fig. 10f). Another noticeable difference between the FRC plots is that the 400 to 1000 nm wavelength region (input bands 6 to 156) in FOR004 shows a high frequency of FRC changes, whereas MAD002 shows intense but less frequent variations. The difference could potentially be explained by the significant amounts of iron oxides present in the Undawidgi Supersuite in FOR004. Iron oxides produce a strong and broad electronic absorption in the 900 nm wavelength region.

ASI predictions generated from the PLS modelling produce reasonable correlations between the scalar and the ASI calculated from geochemical analyses above 0.75 (Table 4). However, when plotting the calculated versus the predicted ASI for drill core MAD002, it is shown that ASI values for the High Mg *E*-MORB samples are significantly

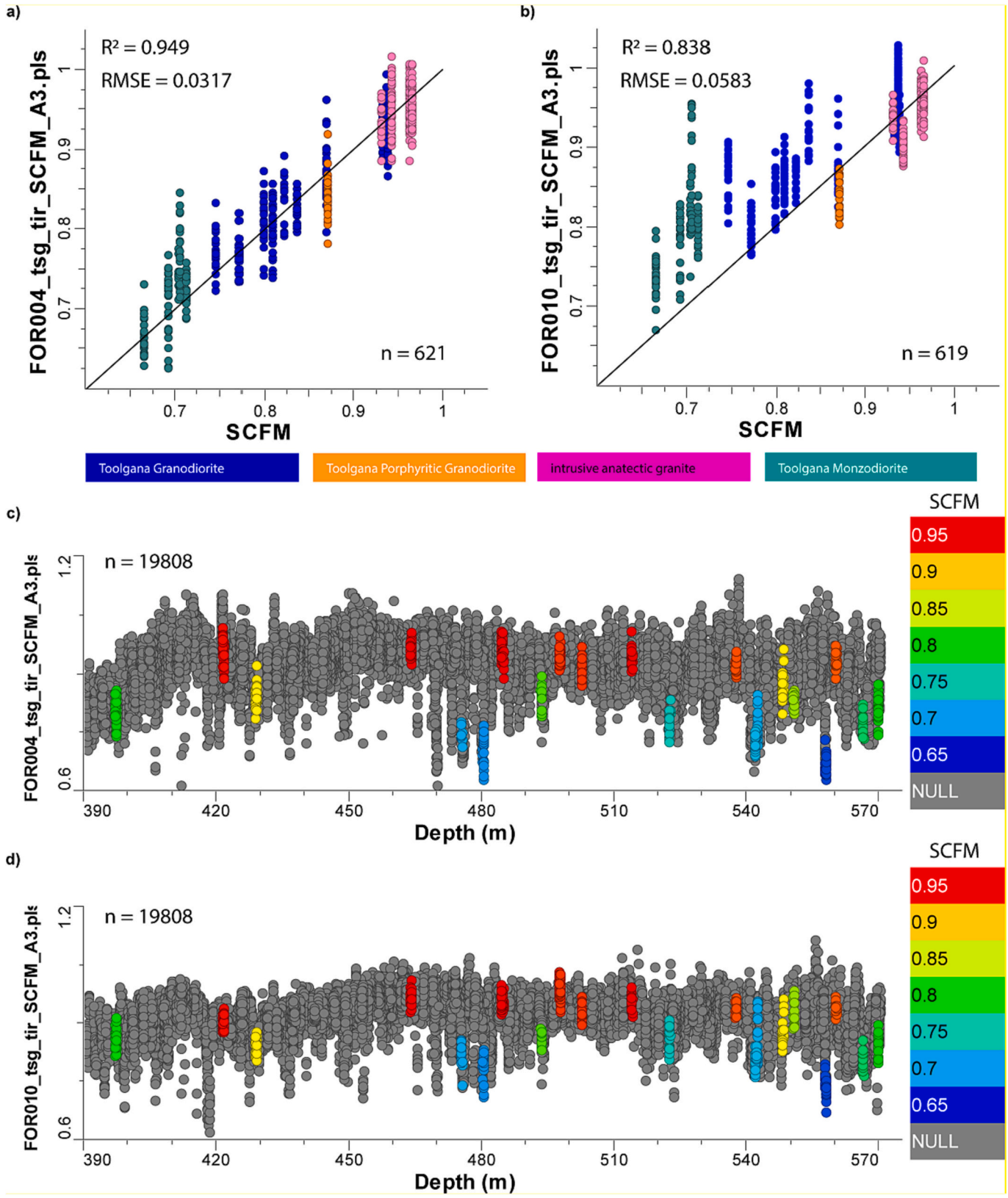

Fig. 9. PLS-modelling results for drill core FOR004: a) Comparison of SCFM calculated from whole rock geochemistry (x-axis) with predicted SCFM using PLS-based scalar developed from FOR004 on the y-axis (FOR004_tsg_tir_SCFM_A3.pls), coloured by rock type. b) Comparison of SCFM calculated from whole rock geochemistry (x-axis) with predicted SCFM using PLS-based scalar developed from FOR010 on the y-axis (FOR010_tsg_tir_SCFM_A3.pls), coloured by rock type. c) Downhole plot (x-axis) of predicted SCFM using FOR004_tsg_tir_SCFM_A3.pls, coloured by SCFM calculated from whole rock geochemistry. d) Downhole plot (x-axis) of predicted SCFM using FOR010_tsg_tir_SCFM_A3.pls, coloured by SCFM calculated from whole rock geochemistry.

Table 4
FOR004 and MAD002 input parameters for ASI. TSG™-files containing the PLS-models can be found in (Laukamp, 2021).

Preparation stage			Calibration stage				Prediction stage	
Drill core	Wave-length range [nm] for cross-validation	Value range	Number of calibration / test spectra	Factors	Coefficient of determi-nation	SEP	Correlation between PLS scalar and measured values	RMSE
FOR004	350–2500 nm	0.156–0.261	321 / 261	16	0.713	0.0169	0.828	0.0184
MAD002	350–2500 nm	0.051–0.220	254 / 163	11	0.865	0.0141	0.756	0.027
MAD002	6500–14,500 nm	0.051–0.220	240 / 223	13	0.932	0.0125	0.819	0.026

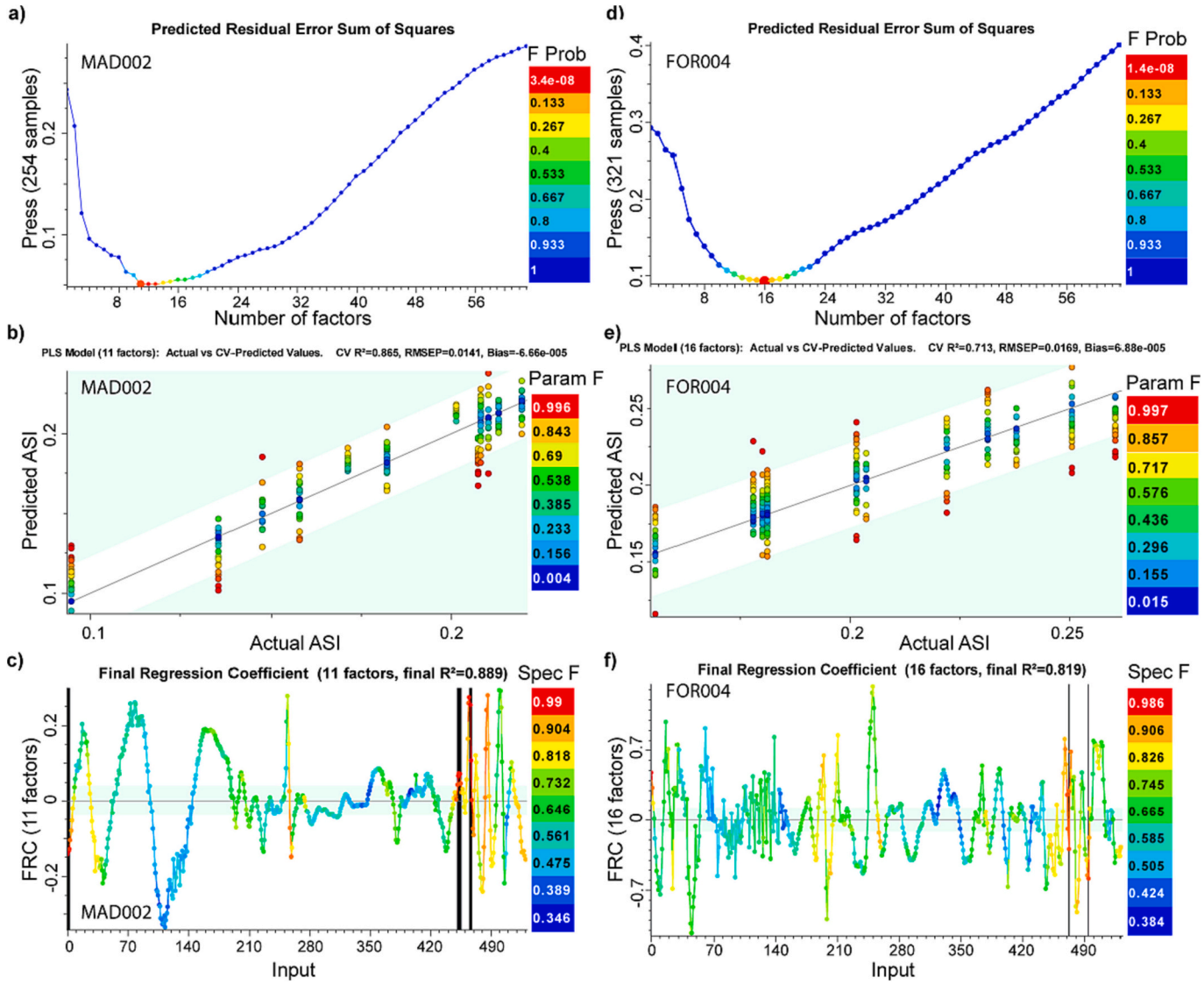

Fig. 10. Calibration stage of the PLS modelling of ASI for drill cores MAD002 and FOR004: a) and d) Ideal number of factors from Predicted Residual Error Sum of Squares (PRESS). b) and e) Comparison of actual and predicted ASI values for assayed intervals. c) and f) SWIR wavelengths of most importance based on Final Regression Coefficient (FRC).

overestimated (Fig. 11b). For MAD002, the predictive ASI scalar produced from VNIR-SWIR spectra can only be applied to E-MORB and Haig Cave Adakite. Because of this, it was attempted to model the ASI for MAD002 using the TIR wavelength range. The PLS modelling produces a reasonable correlation of 0.823 between the scalar and the ASI calculated from geochemical analyses (Table 4). However, plotting the calculated versus the TIR-based predictions of the ASI for drill core MAD002 shows the same insufficient modelling results as for the VNIR-SWIR based modelling, characterised by a significant spread of predicted ASI values.

In summary, the accuracy of these PLS-based modelling of the ASI is strongly related to the number of samples selected for calibration, as well as the abundances of controlling minerals. The most accurate modelling results were achieved for drill core FOR004, where dark and white micas were abundant, and had a strong controlling influence on the ASI. The poorest results were from the mafic rocks of MAD002. This dataset had the smallest sample number of calibration samples, with the low abundance of white mica and plagioclase controlling the ASI.

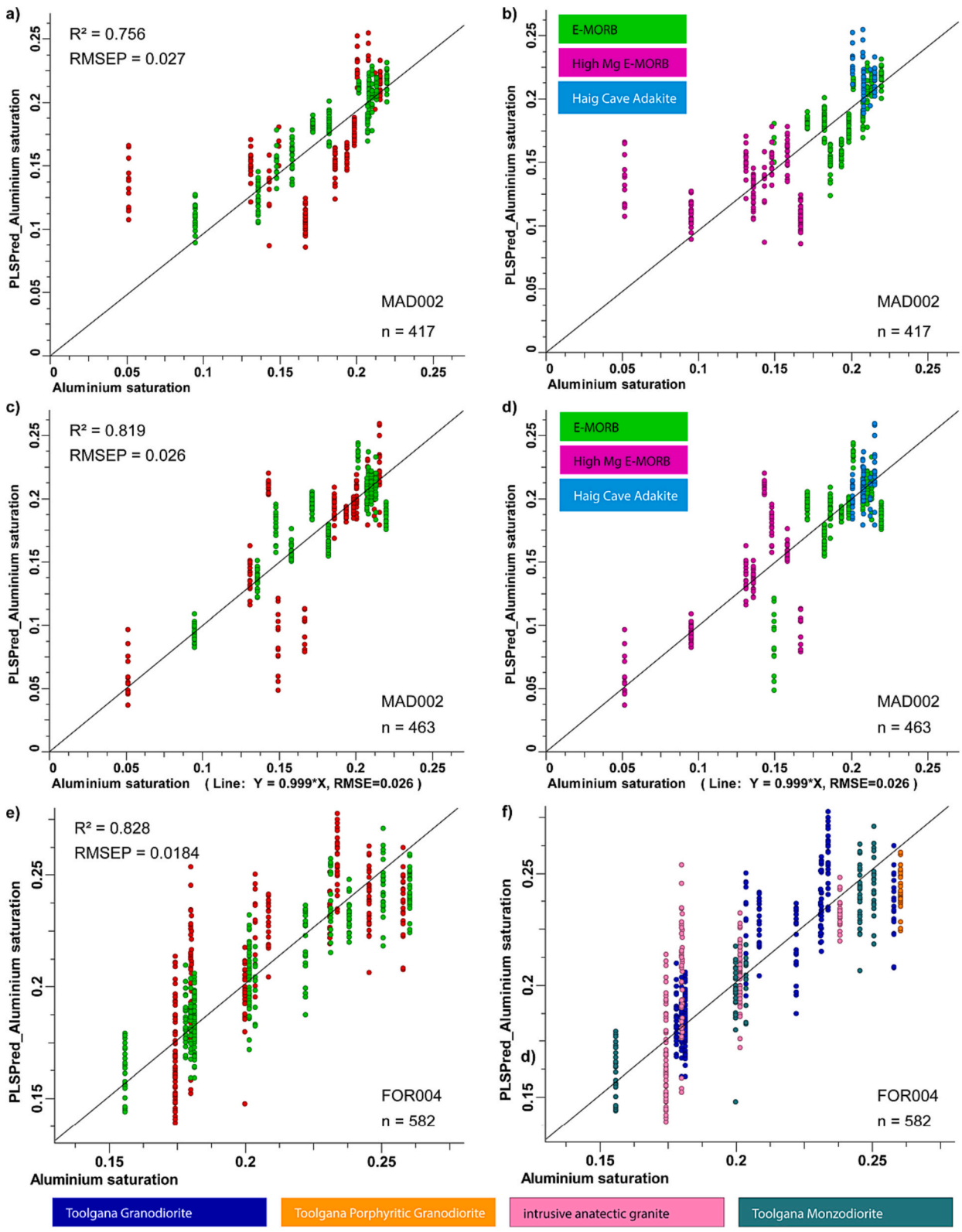

Fig. 11. PLS modelling results of ASI for drill cores MAD002 and FOR004: a) and b) MAD002 VNIR-SWIR wavelength range. c) and d) MAD002 TIR wavelength range. e) and f) FOR004 VNIR-SWIR wavelength range. All plots show actual ASI on x-axis and predicted ASI on y-axis. a), c) and e) coloured by samples selected for training ("on", green) and testing ("off", red). B), d), f) coloured by rock type. (For interpretation of the references to colour in this figure legend, the reader is referred to the web version of this article.)

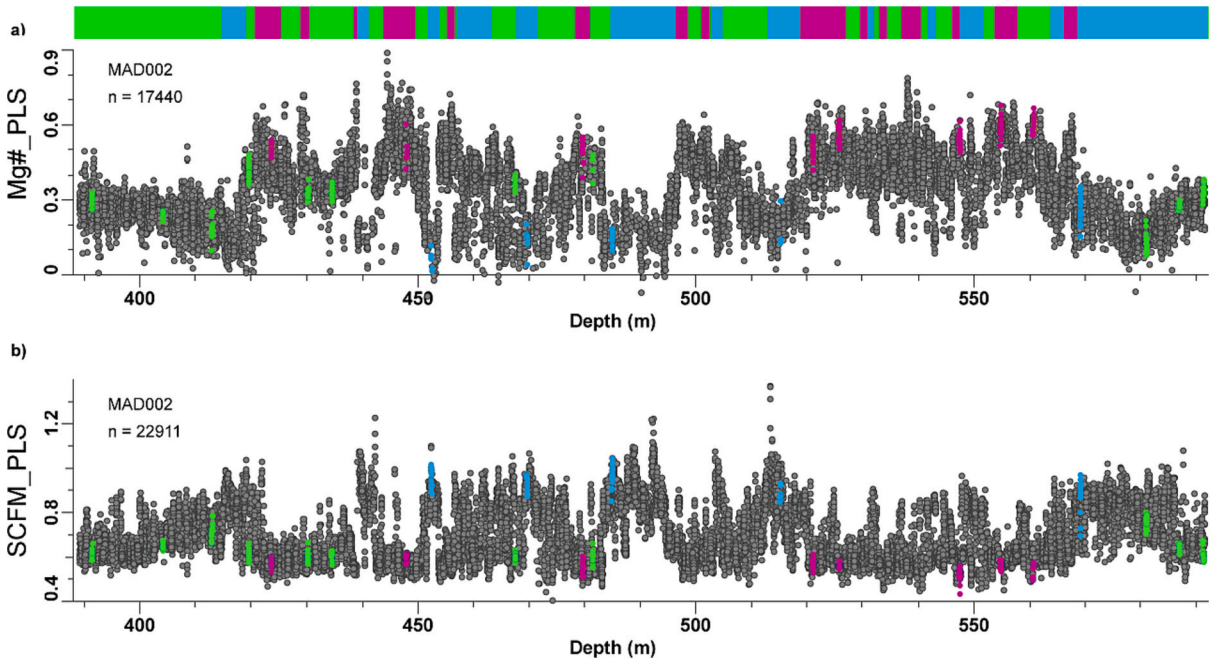

Fig. 12. Downhole plots of drill core MAD002 (interval 390 to 590 m depth): Top colour bar: domains of E-MORB (green), high E-MORB (pink) and adakite (blue) inferred from PLS modelling results; Middle: PLS-modelled SCFM; Bottom: PLS modelled Mg#. The middle and bottom plots coloured by rock types logged by GSWA. (For interpretation of the references to colour in this figure legend, the reader is referred to the web version of this article.)

5. Summary and discussion

PLS-based modelling of the Mg# from VNIR-SWIR reflectance spectra of drill core MAD002 delivered a high correlation between the measured and modelled Mg# (i.e. $R^2 > 0.9$) at an acceptable RMSE (about 10 % of maximum Mg#) when using all samples with available geochemistry for calibration or only half of the samples. The modelled Mg# was a successful descriptor to distinguish between and predict rock types in MAD002, where it was strongly controlled by both amphibole and Mg-rich chlorite. PLS-modelling maximised the key absorption features of both. Application of the most accurate scalar to an unrelated set of rocks (FOR004 and FOR010) was trialled, resulting in correlations between actual and predicted values of $R^2 = 0.71$ and $R^2 = 0.79$, respectively. One set of outliers from the correlation appeared to be due to the iron contribution from sulphides in the samples.

PLS-based modelling of the SCFM was only successful when using TIR reflectance spectra, because major mineral species that contain the respective geochemical elements, such as quartz and feldspar are active in the TIR but not in the VNIR or SWIR wavelength ranges. For drill core FOR010, good SCFM modelling results were achieved with final R^2 of up to 0.965 at acceptable RMSE when comparing measured with the modelled values. Modelling of the SCFM for drill cores FOR004 and MAD002 achieved similar results, suggesting that the PLS-based modelling of SCFM from TIR reflectance spectra delivers modelled values at a high confidence. A downhole plot of the modelled SCFM values of drill core FOR004 highlighted drill core intervals of very low and very high SCFM values that were not sampled by GSWA for whole rock geochemistry, but that could probably be assigned to the Toolgana Monzodiorite and the Intrusive Anatectic Granite, respectively (Fig. 5). Other outliers in downhole plots of the modelled SCFM values typically represent veins or other sample intervals anomalous to the major rock types in the respective drill core.

The PLS-based SCFM scalars developed for drill core FOR010 were applied directly to drill core FOR004, as both drill cores intersect the same lithologies. The modelling results produced a significant correlation ($R^2 = 0.838$) between the SCFM values calculated from whole rock geochemistry analysed in drill core FOR004 compared with the SCFM scalar developed for FOR010. However, the full range of SCFM values modelled for the Toolgana Monzodiorite overlapped with the calculated value ranges of all other three rock types in this drill core. Still, the overall trend of the modelled SCFM in the downhole plot was similar for both PLS-scalars applied to the same drill core FOR004.

The ASI was useful for distinguishing felsic-intermediate datasets where it was strongly controlled by white micas and plagioclase. Plagioclase is only active in the TIR, whereas white mica shows prominent absorption features in both the SWIR and TIR. The VNIR-SWIR and TIR wavelength regions were trialled for modelling the ASI in drill cores MAD002 and FOR004, producing a final R^2 of up to 0.819 at an RMSE of 0.027 and final R^2 of 0.828 at an RMSE of 0.0184, respectively. The accuracy of the produced models was strongly related to the number of samples selected for calibration, as well as the abundances of controlling minerals. ASI-modelling results for drill core FOR004 were highest because both dark and white micas were abundant, and had a strong controlling influence on the ASI. The poorest results were from the mafic rocks of MAD002, where only a few calibration samples were available and where a low abundance of white mica and plagioclase controlled the ASI.

In summary, these experiments have shown that PLS modelling has good potential to fill in gaps between assayed intervals using a flexible approach based on the unique mineral assemblage in each dataset and the key phases controlling any specific geochemical index. In most cases, analyses using all available samples for the calibration dataset were not only more accurate for that specific dataset, but also more accurately applied to unrelated datasets. The most accurate application of PLS-modelling scalars to unrelated datasets occurred when the drill holes had comparable mineral assemblages, meaning the same absorption features influencing the geochemical index for which the model was developed.

It is possible to take this analysis one step further where these descriptors successfully distinguished between rock types and use this to domain the drill hole into separate lithological domains. For example, both the SCFM and Mg# clearly distinguished the adakite from the metabasalt in MAD002 (Fig. 12). Some of these intervals were previously known from the bulk rock geochemistry (coloured points in

Fig. 12), but many were not (grey points). However, there are lot of variations and gradients within the major lithologies and transitions from adakite to *E*-MORB can be gradational too.

6. Conclusions

Geochemistry of three drill cores intersecting the basement of the Eucla basin reported by GSWA was used for training hyperspectral drill core data and develop PLS-based prediction of three geochemical indices: 1) Mg# (Mg/(Mg + Fe)); 2) SCFM (SiO2/(SiO2 + CaO + FeO + MgO)); and 3) ASI (Al2O3/(Na2O + K2O + CaO)). PLS-based modelling of the three geochemical indices achieved a high confidence and the results demonstrate how geochemistry from specific intervals can be matched with hyperspectral data through PLS-based modelling to extrapolate information to non-sampled intervals. The analysis of the FRC across the wavelength range used for the respective PLS model allowed to establish the causative relationship between the hyperspectral and the geochemical data, supporting the evaluation of the robustness of the model, instead of relying only on correlation factors. The PLS-derived scalars developed from one drill core data set were also successfully applied to other drill core data sets, showcasing the potential extrapolation of predicted geochemical indices to other datasets. However, the latter approach only works when the mineral assemblages of the respective drill cores are sufficiently similar.

Declaration of competing interest

The authors declare that they have no known competing financial interests or personal relationships that could have appeared to influence the work reported in this paper.

Data availability

The data discussed in this article are available online at: doi:10.25919/h1cz-dw05 (Laukamp, 2021) or via AuScope's data access portal (http://portal.auscope.org.au/).

Acknowledgements

The authors would like to thank the team at GSWA for their data, and assistance with this project. Catherine Spaggiari and Hugh Smithies from GSWA are thanked for providing samples, background information about the geology and geochemistry of the Eucla Basin. Sincere thanks to Peter Mason, the developer of The Spectral Geologist software, who opened the world of machine learning to spectral geologists.

Emma Beattie was supported by CSIRO Mineral Resources' Discovery program internship scheme and thanks the entire CSIRO spectral sensing team, especially Tom Cudahy, for the support and collective knowledge that makes student internships such a rich learning experience. This work was supported by AuScope's National Virtual Core Library (NVCL) Infrastructure Program, which is funded by AuScope Pty Ltd. and CSIRO Mineral Resources.

CRediT authorship contribution statement

Conceptualization, C.L.; Data curation, E.B., C.L.; Formal analysis, E. B., C.L., M.L.; Funding acquisition, C.L.; Investigation, C.L., E.B., M.L.; Supervision C.L.; Validation, M.L.; Roles/Writing - original draft, E.B., C. L.; Writing - review & editing, C.L.

References

Benbow, M.C., Lindsay, J.M., Alley, N.F., 1995. Eucla Basin and palaeodrainage. In: The Geology of South Australia, Vol 2, The Phanerozoic, Geological Survey of South Australia Bulletin, 54, pp. 178–186.

Chappell, B.W., White, A.J.R., 1992. I- and S-type granites in the Lachlan Fold Belt. Earth Environ. Sci. Trans. R. Soc. Edinburgh 83, 1–26. https://doi.org/10.1017/S0263593300007720.

Conel, J.E., 1969. Infrared emissivities of silicates: Experimental results and a cloudy atmosphere model of Spectral emission from condensed particulate mediums. J. Geophys. Res. 74, 1614–1634. https://doi.org/10.1029/JB074i006p01614.

Day, D., 2021. Handheld Laser Induced Breakdown Spectroscopy (HHLIBS). In: Crocombe, R., Leary, P., Kammrath, B. (Eds.), Portable Spectroscopy and Spectrometry. Wiley, pp. 321–343. https://doi.org/10.1002/9781119636489.ch13.

England, R., 2015. GSWA Petrographic Report on Eucla Basement Stratigraphic Drilling (No. Unpublished).

Haaland, D.M., Thomas, E.V., 1988a. Partial least-squares methods for spectral analyses. 1. Relation to other quantitative calibration methods and the extraction of qualitative information. Anal. Chem. 60, 1193–1202. https://doi.org/10.1021/ac00162a020.

Haaland, D.M., Thomas, E.V., 1988b. Partial least-squares methods for spectral analyses. 2. Application to simulated and glass spectral data. Anal. Chem. 60, 1202–1208. https://doi.org/10.1021/ac00162a021.

Hou, B., Frakes, L.A., Sandiford, M., Worrall, L., Keeling, J., Alley, N.F., 2008. Cenozoic Eucla Basin and associated palaeovalleys, southern Australia — climatic and tectonic influences on landscape evolution, sedimentation and heavy mineral accumulation. Sediment. Geol. 203, 112–130. https://doi.org/10.1016/j.sedgeo.2007.11.005.

Laukamp, C., 2021. TSG Files Contain PLS-scalars Applied to the Eucla Basement Hyperspectral Drill Core Data. https://doi.org/10.25919/H1CZ-DW05.

Laukamp, C., Termin, K.A., Pejcic, B., Haest, M., Cudahy, T., 2012. Vibrational spectroscopy of calcic amphiboles - applications for exploration and mining. ejm 24, 863–878. https://doi.org/10.1127/0935-1221/2012/0024-2218.

Laukamp, C., Beattie, E., LeGras, M., 2021. A Hyperspectral Characterisation of the Eucla Basement Drill Cores (No. EP184011), CSIRO Report.

Laukamp, Carsten, LeGras, M., Lau, I.C., 2021a. Hyperspectral proximal sensing instruments and their applications for exploration through cover. In: Crocombe, R. (Ed.), Portable Spectroscopy and Spectrometry 2: Applications.

Laukamp, Carsten, Rodger, A., LeGras, M., Lampinen, H., Lau, I.C., Pejcic, B., Stromberg, J., Francis, N., Ramanaidou, E., 2021b. Mineral physicochemistry underlying feature-based extraction of mineral abundance and composition from shortwave, mid and thermal infrared reflectance spectra. Minerals 11, 347. https://doi.org/10.3390/min11040347.

Miyashiro, A., 1975. Volcanic rock series and tectonic setting. Annu. Rev. Earth Planet. Sci. 3, 251–269. https://doi.org/10.1146/annurev.ea.03.050175.001343.

Ong, C.C.H., Cudahy, T.J., 2014. Mapping contaminated soils: using remotely-sensed hyperspectral data to predict pH: Remote sensing of contaminated soils. Eur. J. Soil Sci. 65, 897–906. https://doi.org/10.1111/ejss.12160.

Salisbury, J.W., D'Aria, D.M., 1989. Measurement of Christiansen Frequencies in Spectra of Particulate Samples for Determination of Rock Composition, 20, p. 940.

Spaggiari, C.V., Smithies, R.H., 2015. Eucla Basement Stratigraphic Drilling Results Release Workshop: Extended Abstracts, Record. Geological Survey of Western Australia.

Walter, L.S., Salisbury, J.W., 1989. Spectral characterization of igneous rocks in the 8- to 12-μm region. J. Geophys. Res. 94, 9203. https://doi.org/10.1029/JB094iB07p09203.

Zen, E.-A., 1986. Aluminum enrichment in silicate melts by fractional crystallization: some mineralogic and petrographic constraints. J. Petrol. 27, 1095–1117. https://doi.org/10.1093/petrology/27.5.1095.